Supplementary materials

2.1. Sample synthesis

$$Nb_2O_5+13Mo+25MoO_3=40Nb_{0.05}Mo_{0.95}O_2$$

$$3Nb_2O_5+19Mo+35MoO_3=60Nb_{0.1}Mo_{0.9}O_2$$

$$Nb_2O_5+3Mo+5MoO_3=10Nb_{0.2}Mo_{0.8}O_2$$

$$3Nb_2O_5+7Mo+11MoO_3=24Nb_{0.25}Mo_{0.75}O_2$$

$$9Nb_2O_5+17Mo+25MoO_3=60Nb_{0.3}Mo_{0.7}O_2$$

$$3Nb_2O_5+5Mo+7MoO_3=18Nb_{0.33}Mo_{0.67}O_2$$

$$9Nb_2O_5+7Mo+5MoO_3=30Nb_{0.6}Mo_{0.4}O_2$$

$$13Nb_2O_5+9Mo+5MoO_3=40Nb_{0.65}Mo_{0.35}O_2$$
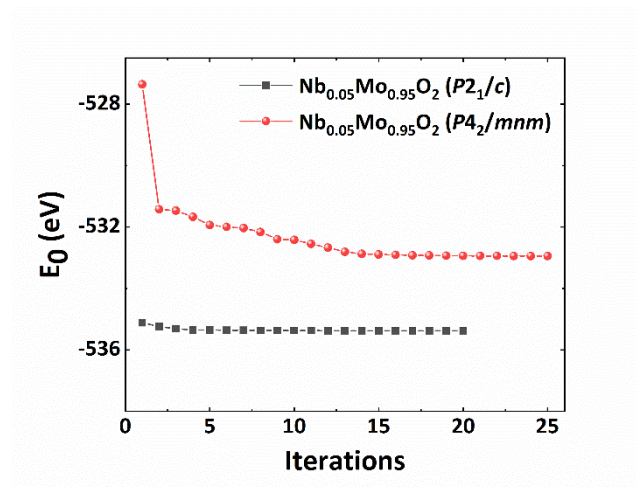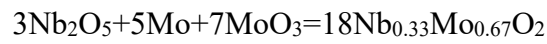
Fig. S1. The calculated energies of $Nb_{0.05}Mo_{0.95}O_2$ with $P2_1/c$ and $P4_2/mnm$ space groups, respectively.

Fig. S1 indicates the calculated energies of $Nb_{0.05}Mo_{0.95}O_2$ with two different space groups: $P2_1/c$ and $P4_2/mnm$. We perform the first-principles calculations within the

local spin-density approximation as implemented in the Vienna Ab-initio Simulation Package (VASP) [1, 2]. The projector-augmented wave method is used and the cutoff energy is 500 eV [3]. The atomic positions are relaxed using the conjugate gradient algorithm until the residual forces are smaller than 0.02 eV/Å [4]. A $1 \times 7 \times 7$ Gamma k-mesh is used for relaxation. We used space group $P4_2/mnm$ of $NbMoO_4$ and space group $P2_1/c$ of MoO_2 as the basic structures to construct superlattices for $Nb_{0.05}Mo_{0.95}O_2$ and calculated the binding energies. The results show that when $Nb_{0.05}Mo_{0.95}O_2$ adopts the space group of $P2_1/c$, the energy of the system is lower, consistent with the XRD results.
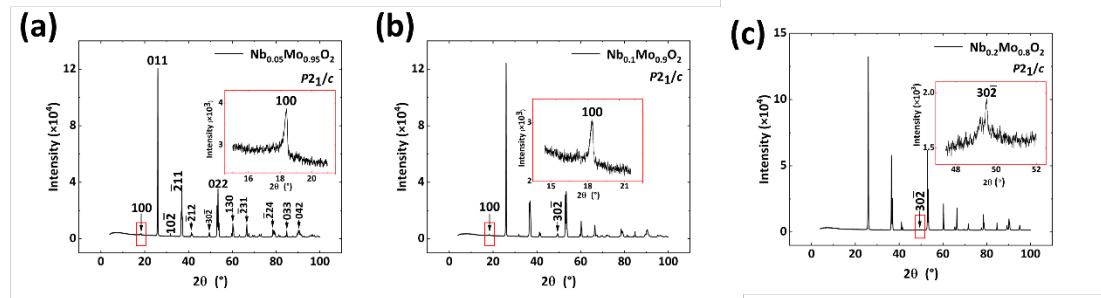
Fig. S2. The XRD patterns of $Nb_{0.05}Mo_{0.95}O_2$, $Nb_{0.1}Mo_{0.9}O_2$, and $Nb_{0.2}Mo_{0.8}O_2$ with the specific peaks of the $P2_1/c$ highlighted in red rectangular boxes.

Fig. S2 displays the XRD patterns of $Nb_{0.05}Mo_{0.95}O_2$ (Fig. S2 (a)), $Nb_{0.1}Mo_{0.9}O_2$ (Fig. S2 (b)), and $Nb_{0.2}Mo_{0.8}O_2$ (Fig. S2 (c)). The red rectangular boxes indicate the specific peaks of the $P2_1/c$ structure, corresponding to the (100) peak for $Nb_{0.05}Mo_{0.95}O_2$ and $Nb_{0.1}Mo_{0.9}O_2$ and the (30$\bar{2}$) peak for $Nb_{0.2}Mo_{0.8}O_2$. However, for $Nb_{0.2}Mo_{0.8}O_2$, the (100) peak disappears and the intensity of the (30$\bar{2}$) peak significantly weakens.
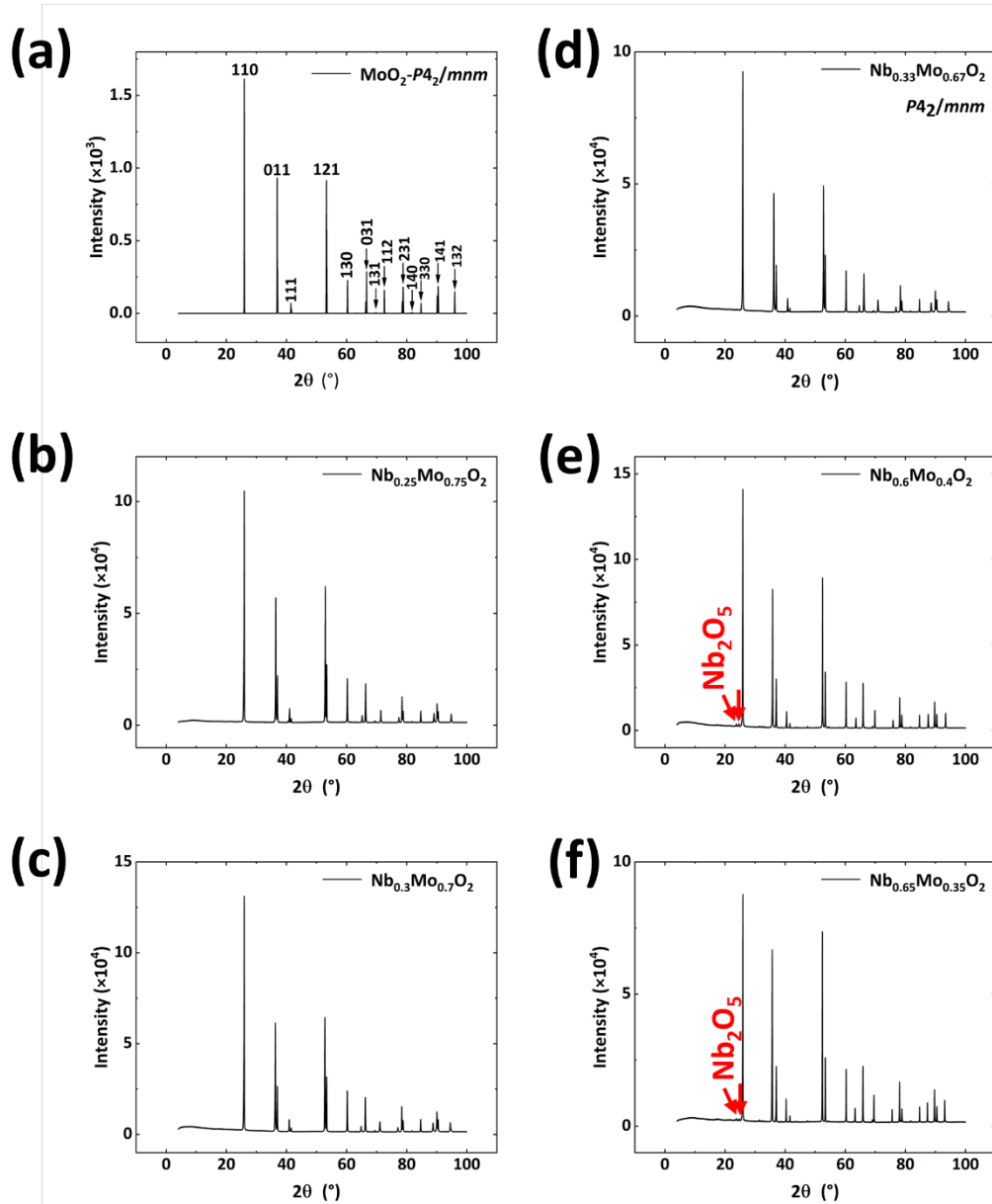
Fig. S3. The XRD patterns of MoO_2 ($P4_2/mnm$) and $Nb_xMo_{1-x}O_2$ (x=0.25, 0.3, 0.33, 0.6, 0.65).

Fig. S3 presents the simulated XRD pattern of MoO_2 ($P4_2/mnm$) (Fig. S3 (a)) and the XRD patterns of $Nb_xMo_{1-x}O_2$ (x=0.25, 0.3, 0.33, 0.6, 0.65) (Fig. S3 (b), (c), (d), (e), and (f)). Comparing the XRD patterns of $Nb_xMo_{1-x}O_2$ (x=0.25, 0.3, 0.33, 0.6, 0.65) with the simulated XRD pattern of MoO_2 ($P4_2/mnm$), no significant differences are observed.

However, for x=0.25 and 0.3 compositions, the compounds exhibit $I4_1/a$ structure, while for x=0.33, 0.6, and 0.65 compositions, the compounds adopt the $P4_2/mnm$ structure, as confirmed by SAED analyses. Notably, the synthesized compounds with x=0.6 and 0.65 compositions exhibit Nb_2O_5 impurity phase, marked by the red arrows in Fig. S3.
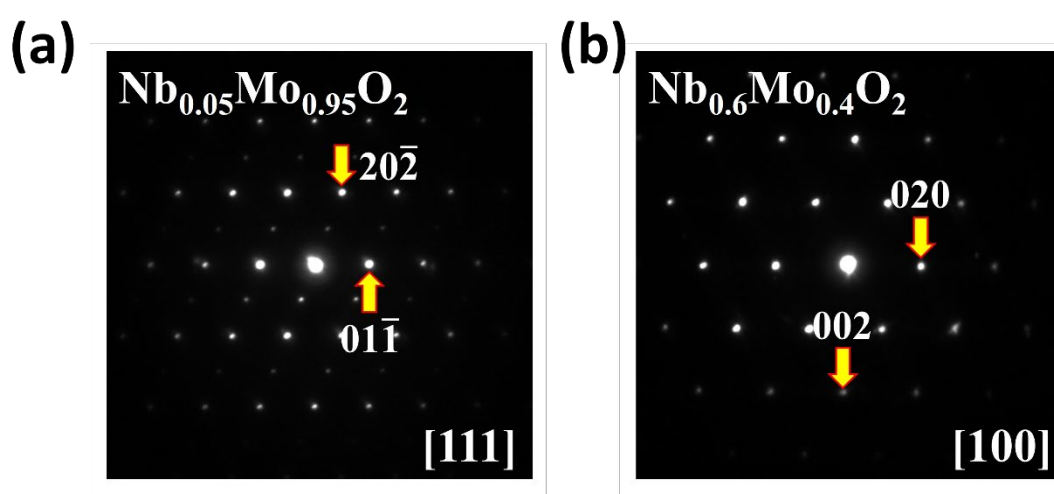
Fig. S4. The SAED patterns of $Nb_{0.05}Mo_{0.95}O_2$ along the [111] direction and $Nb_{0.6}Mo_{0.4}O_2$ along the [100] direction.

Fig. S4 (a) displays the SAED pattern of $Nb_{0.05}Mo_{0.95}O_2$ along the [111] direction, which can be indexed to the $P2_1/c$ structure. Fig. S4 (b) shows the SAED pattern of $Nb_{0.6}Mo_{0.4}O_2$ along the [100] direction, where no superlattice spots are observed unlike in $Nb_{0.25}Mo_{0.75}O_2$. By examining the presence or absence of superlattice spots along the specific zone axes ([100], [111], [113]), we can differentiate the structures between $I4_1/a$ and $P4_2/mnm$.
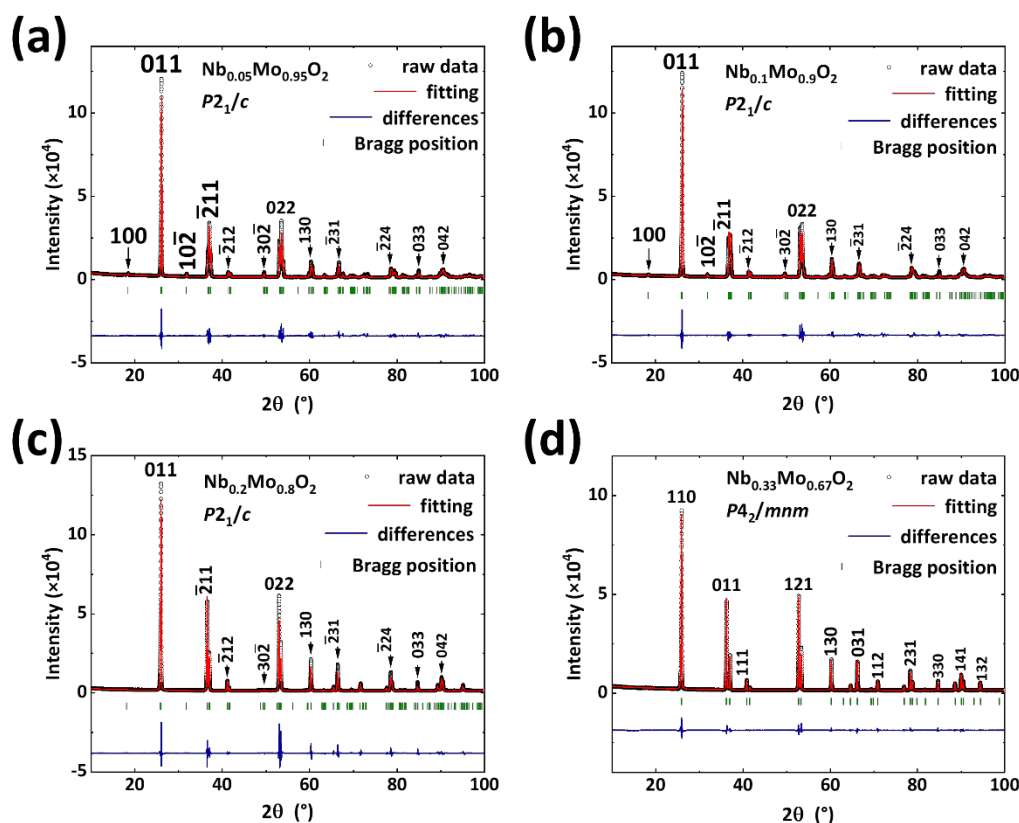
Fig. S5. The XRD refinement results of $Nb_{0.05}Mo_{0.95}O_2$, $Nb_{0.1}Mo_{0.9}O_2$, $Nb_{0.2}Mo_{0.8}O_2$, and $Nb_{0.33}Mo_{0.67}O_2$.

Fig. S5 (a), (b), (c), and (d) display the refinement results of $Nb_{0.05}Mo_{0.95}O_2$, $Nb_{0.1}Mo_{0.9}O_2$, $Nb_{0.2}Mo_{0.8}O_2$, and $Nb_{0.33}Mo_{0.67}O_2$, respectively. The refinement results of $Nb_{0.05}Mo_{0.95}O_2$, $Nb_{0.1}Mo_{0.9}O_2$, and $Nb_{0.2}Mo_{0.8}O_2$ reveal that all the three compounds exhibit the $P2_1/c$ structure. The refined structural parameters for these compounds are presented in Table S1. However, for $Nb_{0.2}Mo_{0.8}O_2$, the refined atomic positions deviate a lot from the MoO_2 ($P2_1/c$) structure, indicating that this composition may possess a critical structure between $P2_1/c$ and $I4_1/a$. The refinement results for $Nb_{0.33}Mo_{0.67}O_2$ demonstrate the $P4_2/mnm$ structure, and the refined structural parameters are presented in Table S2.

Table S1 Refinement structural parameters of $Nb_xMo_{1-x}O_2$ (x=0.05, 0.1, 0.2)

Parameters	$Nb_{0.05}Mo_{0.95}O_2$	$Nb_{0.1}Mo_{0.9}O_2$	$Nb_{0.2}Mo_{0.8}O_2$
Lattice system	Monoclinic	Monoclinic	Monoclinic
space group	$P2_1/c$	$P2_1/c$	$P2_1/c$
a (Å)	5.617 (1)	5.632 (1)	5.705 (1)
b (Å)	4.851 (1)	4.846 (1)	4.851 (1)
c (Å)	5.624 (1)	5.617 (1)	5.635 (1)
β (°)	120.93 (1)	120.94 (1)	120.50 (1)
Atomic position	(x, y, z)	(x, y, z)	(x, y, z)
Mo (Nb)	0.234 (1), 0.006 (1), 0.017 (1)	0.236 (1), 0.011 (1), 0.014 (1)	0.247 (2), -0.001 (1), 0.001 (1)
O1	0.102 (6), 0.180 (4), 0.206 (3)	0.087 (2), 0.231 (2), 0.234 (2)	0.103 (2), 0.198 (3), 0.171 (4)
O2	0.390 (1), 0.640 (3), 0.218 (4)	0.458 (2), 0.596 (3), 0.335 (1)	0.353 (3), 0.787 (2), 0.316 (2)
R_{wp} (%)	10.5	9.65	13.3
R_p (%)	6.79	6.30	8.07

Table S2 Refinement structural parameters of $Nb_{0.33}Mo_{0.67}O_2$

Parameters	$Nb_{0.33}Mo_{0.67}O_2$
Lattice system	Tetragonal
space group	$P4_2/mnm$
a (Å)	4.851 (1)
b (Å)	4.851 (1)
c (Å)	2.880 (1)
Atomic position	(x, y, z)
Nb (Mo)	0, 0, 0
O	0.293 (1), 0.293 (1), 0
R_{wp} (%)	5.40
R_p (%)	3.78
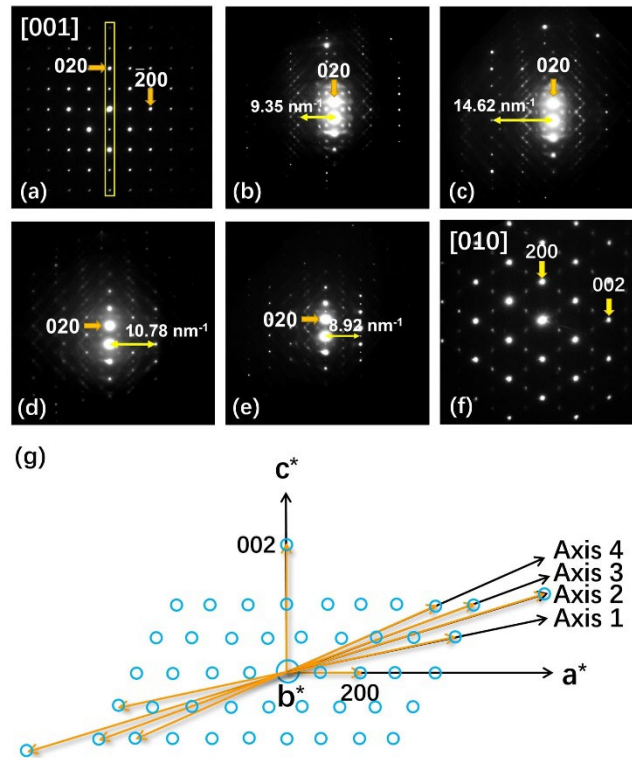
Fig. S6. (a) The SAED pattern of $Nb_{0.25}Mo_{0.75}O_2$ along the [001] zone axis. (b), (c), (d), and (e) The SAED patterns with crystal rotations. (f) The SAED pattern along the [010] direction. (g) Constructed a^*c^* crystal plane based on the above experimental SAED patterns.
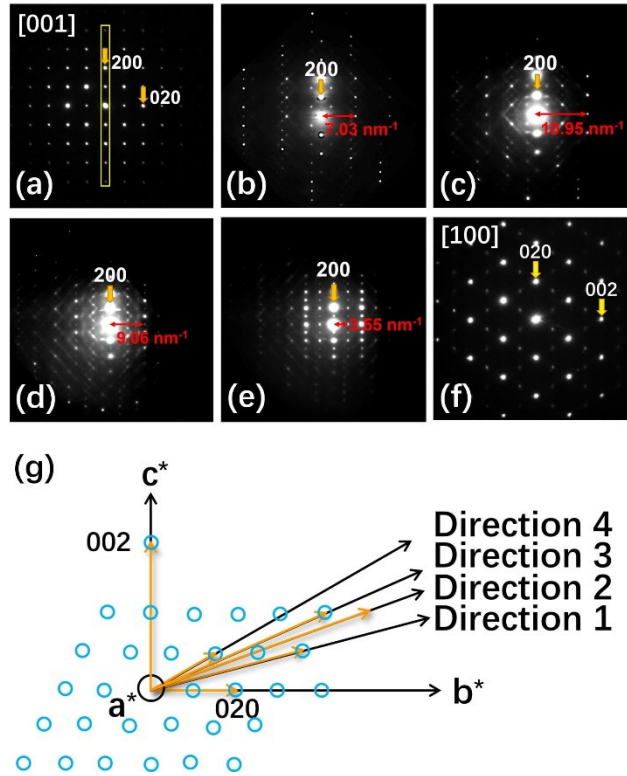
Fig. S7. (a) The SAED pattern of $Nb_{0.25}Mo_{0.75}O_2$ along the [001] zone axis. (b), (c), (d), and (e) The SAED patterns with crystal rotations. (f) The SAED pattern along the [100] direction. (g) Constructed b^*c^* crystal plane based on the above experimental SAED patterns.

In Figs. S6 and S7, we obtain the SAED patterns along the [001] direction. We fix the plane (010)/(100) and rotate the TEM specimen. We gain SAED patterns along the different zone axes (Fig. S6/S7 (b), (c), (d), and (e)). We measure the distance between the diffraction and transmission spots and draw the schematic plane a^*c^* (b^*c^*) in Fig. S6/S7 (g). Besides, we conclude the periodicity and expand the spots. The reciprocal a^*c^* (b^*c^*) plane and the reciprocal lattice are gained.
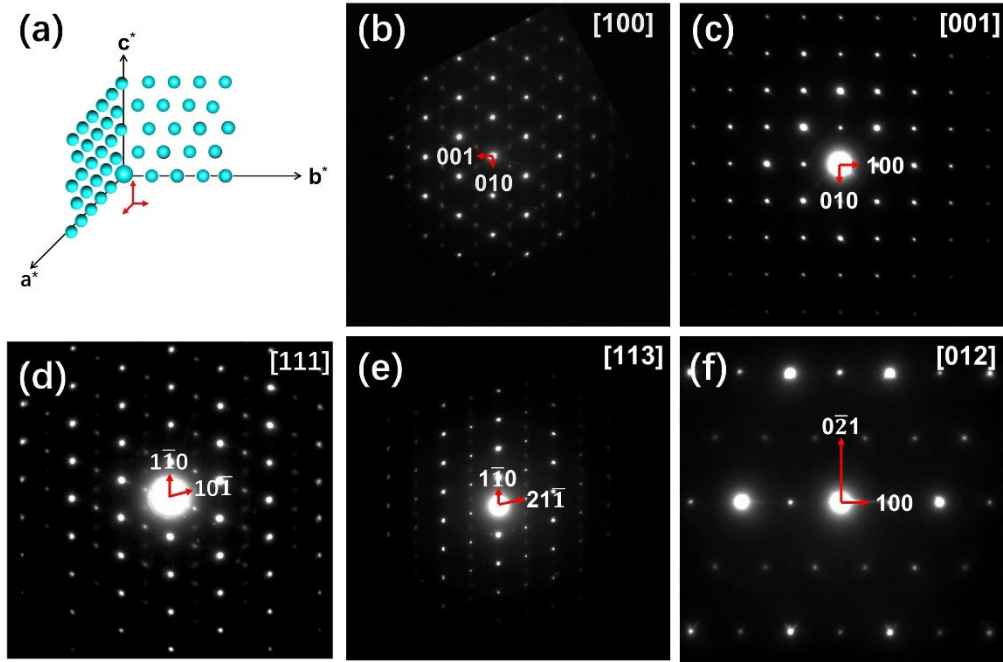
Fig. S8. (a) The schematic reciprocal lattice of $Nb_{0.25}Mo_{0.75}O_2$. (b), (c), (d), (e), (f), and (g) The experimental SAED patterns of $Nb_{0.25}Mo_{0.75}O_2$ along the [100], [001], [111], [113], and [012] zone axes, respectively. The SAED patterns are indexed by using new lattice parameters.

According to the reciprocal lattice, the new lattice constants of $Nb_{0.25}Mo_{0.75}O_2$ are determined as $a=b=9.699$ Å and $c=5.686$ Å (tetragonal). As shown in Fig. S8, we conclude the reflection conditions and determine space group $I4_1/a$.
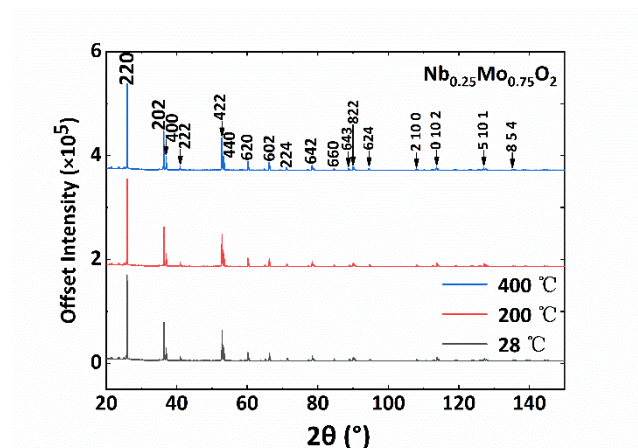
Fig. S9. The temperature-variable XRD patterns of $Nb_{0.25}Mo_{0.75}O_2$ at 28 °C, 200 °C and 400 °C, respectively.

The temperature variable XRD patterns of $Nb_{0.25}Mo_{0.75}O_2$ at 28 °C (black line), 200 °C (red line) and 400 °C (blue line), respectively are displayed in Fig. S9. We index the XRD patterns with lattice parameters $a=b=9.71$ Å, $c=5.68$ Å. The XRD pattern from 20° to 150° shows no structural transition. Therefore, $Nb_{0.25}Mo_{0.75}O_2$ keeps body-centered tetragonal ($I4_1/a$) structure from room temperature to 400 °C.
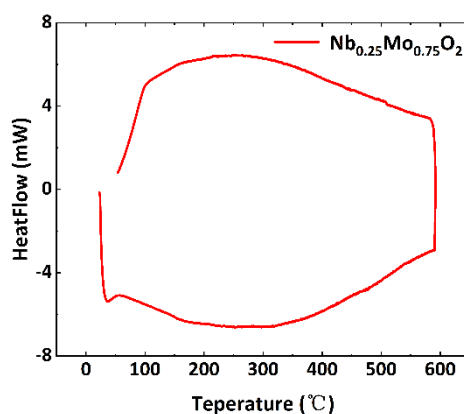
Fig. S10. The DSC results of $Nb_{0.25}Mo_{0.75}O_2$ in the temperature range of room temperature-600 °C.

11

We performed thermal analysis on $Nb_{0.25}Mo_{0.75}O_2$ using a Differential Scanning Calorimeter (model DSC131 Evo). The Differential Scanning Calorimetry results demonstrate that no phase transformation characteristics is observed for $Nb_{0.25}Mo_{0.75}O_2$, indicating the stability of the structure in the temperature range of room temperature-600 °C, consistent with the temperature-variable XRD results.

References

[1] S. L. Dudarev, G. A. Botton, S. Y. Savrasov, C. J. Humphreys, A. P. Sutton, Electron-energy-loss spectra and the structural stability of nickel oxide: An LSDA+ U study, Phys. Rev. B. 57 (1998) 1505.

[2] G. Kresse, J. Furthmüller, Efficient iterative schemes for ab initio total-energy calculations using a plane-wave basis set, Phys. Rev. B. 54 (1996) 11169.

[3] G. Kresse, D. Joubert, From ultrasoft pseudopotentials to the projector augmented-wave method, Phys. Rev. B. 59 (1999) 1758.

[4] W. Press, Numerical recipes 3rd edition: The art of scientific computing, Cambridge University Press, NY, USA 2007.